

Numerical evaluation of mean-field homogenisation methods for predicting shale elastic response

M. Goodarzi · M. Rouainia · A. C. Aplin

Received: date / Accepted: date

Abstract Homogenisation techniques have been successfully used to estimate the mechanical response of synthetic composite materials, due to their ability to relate the macroscopic mechanical response to the material microstructure. The adoption of these mean-field techniques in geo-composites such as shales is attractive, partly because of the practical difficulties associated with the experimental characterisation of these highly heterogeneous materials. In this paper, numerical modelling has been undertaken to investigate the applicability of homogenisation methods in predicting the macroscopic, elastic response of clayey rocks. The rocks are considered as two-level composites consisting of a porous clay matrix at the first level and a matrix-inclusion morphology at the second level. The simulated microstructures ranged from a simple system of one inclusion/void embedded in a matrix to complex, random microstructures. The effectiveness and limitations of the different homogenisation schemes were demonstrated through a comparative evaluation of the macroscopic elastic response, illustrating the appropriate schemes for upscaling the microstructure of shales. Based on the numerical simulations and existing experimental observations, a randomly distributed pore system for the micro-structure of porous clay matrix has been proposed which can be used for the subsequent development and validation of shale constitutive models and their flow properties. **Finally, the homogenisation techniques were used to predict the experimental measurements of elastic response. The developed methodology is proved to be a valuable too for verifying the accuracy and performance of the homogenisation techniques.**

Keywords Shale · Rock Physics · Homogenisation · Material Point Method

M. Goodarzi

School of Civil Engineering and Geosciences, Newcastle University, Newcastle upon Tyne NE1 7RU, UK

M.Rouainia

School of Civil Engineering and Geosciences, Newcastle University, Newcastle upon Tyne NE1 7RU, UK

A.C.Aplin

Department of Earth Science, Durham University, DH1 3LE, UK

1 Introduction

The prediction of the mechanical behaviour of clayey rocks such as shales is of great importance as these materials play key roles as barriers to fluid flow in a range of geological and engineering applications such as seals to hydrocarbon reservoirs and CO₂ storage sites, and also as nuclear waste repositories. There is a surprising lack of experimental geomechanical data on well-characterised shales, which are nevertheless essential for populating numerical models with which to predict the mechanical response of shales subjected to changes in the stress regime as a result, for example, of hydrocarbon production or CO₂ injection. This is due in part to difficulties in obtaining well-preserved core samples and the cost and time involved in conventional rock mechanics laboratory testing. Furthermore, shales are compositionally heterogeneous at different scales, which creates difficulties in relating macroscopic (e.g. centimetre-scale) properties to the micron to millimetre heterogeneities which characterise shales and which are commonly observed under the microscope.

An alternative approach to estimating mechanical response of composite materials is to use homogenisation techniques, which have been successfully applied to synthetic composite materials to account for microstructural arrangements, volume fractions and material properties of defined constituents such as a matrix and inclusions within that matrix. In order to obtain close-form solutions for the macroscale behaviour of composite materials, assumptions and simplifications are required about inclusion shapes, the interaction between the matrix and inclusions and the interaction between adjacent inclusions. The nature of these assumptions has resulted in a range of homogenization schemes, of which the most popular are the Dilute Scheme (DS), the Mori-Tanaka (MT), the Self-Consistent Scheme (SCS) and the Generalized Self-Consistent Scheme (GSCS) [28, 17, 47, 5].

Direct numerical simulations based on microstructural information have been used not only to provide insights into the overall macroscopic behaviour of multi-phase media, but also to quantify the applicability and limitations of the different homogenisation techniques [16, 22, 29, 30, 35, 36, 40, 49]. Studies to date have considered synthetic composite materials with a matrix containing less than 20% of spherical or cylindrical inclusions; void spaces in the matrix have been assumed to

be spherical, isolated pores. Results demonstrate that the accuracy of the homogenisation techniques is sensitive to the volume fraction and the shape of inclusions, along with the stiffness contrast between the inclusions and the matrix.

Shale, a natural geo-composite is inherently more complex than a synthetic materials but can be considered a two-step composite (Figure 1). Shale comprises (a) mineral inclusions (e.g. quartz, feldspar, pyrite, calcite) which are highly variable in both volume fraction and shape, and (b) a clay matrix which contains randomly distributed voids. The material properties of the clay matrix, which consists of micron-size clay minerals and sub-micron-size voids, are difficult to quantify. Homogenisation methods have thus been used in conjunction with various assumptions to characterise the mechanical behaviour of both shales and the solid unit of clay [18, 20, 14, 33, 15, 50, 37, 38, 44]. **Hornby et al. [18] assumed elliptical clay particles and used the differential effective medium (DEM) approach to upscale shale properties. Shen et al. [37] considered pore spaces as spherical, isolated voids and adopted the MT scheme at both levels of homogenisation. In contrast, Bobko and Ulm [7] proposed a model for nano-granular material with coaxial anisotropic elastic grains for the clay matrix. Ortega et. al. [33] adopted the concept and implemented SCS in homogenising shale microstructure.**

In this paper, we undertake numerical investigations designed to develop a better understanding of the capabilities and limitations of the homogenisation methods as a way of predicting the macroscopic behaviour of shales. Several numerically-generated microstructure at both level of clayey rocks composite based on SEM images and stochastic models were simulated for this purpose. The macroscopic elastic response of these models were compared with the values predicted by the homogenisation methods accounting for their microstructures. Finally, the model predictions were compared with experimental measurements to shed light on the efficacy and limitations of each homogenisation technique.

2 Mean-field homogenisation methods

In order to characterize the macroscopic response of a multi-phase composite, a representative element volume (REV) is required. This volume (Ω) is defined in such a way that the macroscopic response for any sample larger than the REV will

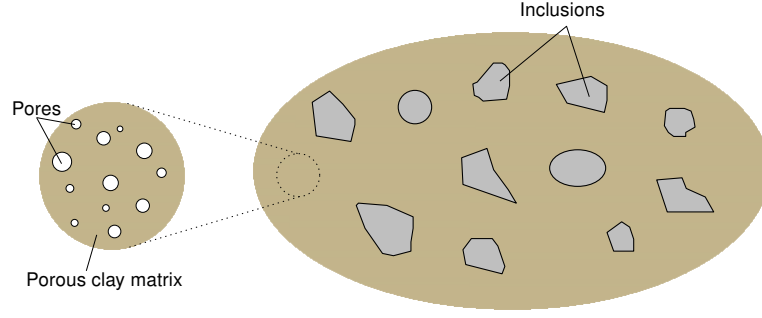


Fig. 1 Schematic microstructure of shales.

be independent of the sample size. Assuming a linear elastic response for all the composite constituents, the elastic relationship at both micro and macro scales can be described as:

$$\boldsymbol{\sigma}(\boldsymbol{x}) = \mathbb{C}(\boldsymbol{x}) : \boldsymbol{\varepsilon}(\boldsymbol{x}) \quad (1)$$

$$\boldsymbol{\Sigma} = \mathbb{C}_{\text{hom}} : \boldsymbol{E} \quad (2)$$

where \boldsymbol{x} is the position vector inside the REV, $\boldsymbol{\sigma}(\boldsymbol{x})$ is the local stress field, $\boldsymbol{\varepsilon}(\boldsymbol{x})$ is the local strain field, $\boldsymbol{\Sigma}$ is the macroscopic stress tensor and \boldsymbol{E} is the macroscopic strain tensor. $\mathbb{C}(\boldsymbol{x})$ and \mathbb{C}_{hom} represent the local and global fourth-order stiffness tensors, respectively.

If the average of a field, α , over the representative element volume is defined as:

$$\langle \alpha \rangle = \frac{1}{\Omega} \int_{\Omega} \alpha(\boldsymbol{x}) d\boldsymbol{x} \quad (3)$$

the macroscopic stress and strain can then be written in the following form:

$$\boldsymbol{\Sigma} = \langle \boldsymbol{\sigma} \rangle \quad ; \quad \boldsymbol{E} = \langle \boldsymbol{\varepsilon} \rangle \quad (4)$$

In order to relate the macroscopic strain to the local strain field, a linear relationship can be established as:

$$\boldsymbol{\varepsilon}(\boldsymbol{x}) = \mathbb{A}(\boldsymbol{x}) : \boldsymbol{E} \quad (5)$$

where \mathbb{A} is the localization tensor which depends on both the homogenisation scheme and the assumptions made on the mechanical response. Considering a composite with N different phases and combining Eq. 5 into Eq. 4, it can be shown that:

$$\langle \mathbb{A} \rangle = \sum_{r=0}^N f_r \langle \mathbb{A}_r \rangle = \mathbb{I} \quad (6)$$

where f_r and \mathbb{A}_r represent the volume fraction and localization tensor for phase r , respectively. Consequently, the relationship between the macroscopic stress and strain can be determined.

$$\boldsymbol{\sigma}(\mathbf{x}) = \mathbb{C}(\mathbf{x}) : \mathbb{A}(\mathbf{x}) : \mathbf{E} \quad (7)$$

$$\boldsymbol{\Sigma} = \langle \boldsymbol{\sigma} \rangle = \langle \mathbb{C} : \mathbb{A} \rangle : \mathbf{E} \quad (8)$$

$$\mathbb{C}_{\text{hom}} = \langle \mathbb{C} : \mathbb{A} \rangle = \sum_{r=0}^N f_r \mathbb{C}_r : \mathbb{A}_r \quad (9)$$

where \mathbb{C}_r is the stiffness tensor for phase r . If the continuous phase representing the composite matrix which surrounds the remaining constituents (see Figure 1) is assigned as phase 0, Eq. 9 can be re-written as:

$$\mathbb{C}_{\text{hom}} = \mathbb{C}_0 + \sum_{r=1}^N f_r (\mathbb{C}_r - \mathbb{C}_0) : \mathbb{A}_r \quad (10)$$

The analytical expression for both the localization tensor and the effective homogenised stiffness tensor will be summarised for each of the four homogenisation schemes adopted in this study, namely the Dilute Scheme, the Mori-Tanaka model (MT), the Self-Consistent Scheme (SCS), and the Generalized Self-Consistent Scheme (GSCS). For more information on the derivations and assumptions of these schemes readers are referred to Zaoui [47], Chateau and Dormieux [9], Benveniste [5] and Guery *et al.* [15].

2.1 Dilute Scheme

In the Dilute Scheme, the primary assumption is that the concentration of inclusions in the matrix is small so that there is no interaction between them and their separation is well-defined. This leads to a solution for composites with low concentrations of inclusions based on a single inclusion embedded in an infinite matrix. In this case, the localisation tensor for phase r can be defined as follows:

$$\mathbb{A}_r = [\mathbb{I} + \mathbb{P}_{I_r}^0 : (\mathbb{C}_r - \mathbb{C}_0)]^{-1} \quad (11)$$

where $\mathbb{P}_{I_r}^0$ is the Hill's tensor which is related to the Eshelby tensor and is in general a function of the shape and orientation of the r th inclusion as well as the stiffness tensor of the matrix phase (see Appendix A1). The corresponding homogenised stiffness tensor can be derived as:

$$\mathbb{C}_{\text{hom}} = \mathbb{C}_0 + \sum_{r=1}^N f_r [(\mathbb{C}_r - \mathbb{C}_0)^{-1} + \mathbb{P}_{I_r}^0]^{-1} \quad (12)$$

2.2 Mori-Tanaka Scheme

The Mori-Tanaka model was developed in a similar way as the Dilute Scheme by including an extra term in order to account for the interaction between inclusions. In this case, the localisation tensor, \mathbb{A}_r , was given as:

$$\mathbb{A}_r = [\mathbb{I} + \mathbb{P}_{I_r}^0 : (\mathbb{C}_r - \mathbb{C}_0)]^{-1} : \left[\sum_{s=0}^N f_s [\mathbb{I} + \mathbb{P}_{I_r}^0 : (\mathbb{C}_s - \mathbb{C}_0)]^{-1} \right]^{-1} \quad (13)$$

and the corresponding homogenised effective stiffness tensor can be obtained as:

$$\mathbb{C}_{\text{hom}} = \mathbb{C}_0 + \sum_{r=1}^N f_r [(\mathbb{C}_r - \mathbb{C}_0)^{-1} + \mathbb{P}_{I_r}^0]^{-1} \left[\sum_{s=0}^N f_s [\mathbb{I} + \mathbb{P}_{I_r}^0 : (\mathbb{C}_s - \mathbb{C}_0)]^{-1} \right]^{-1} \quad (14)$$

2.3 Self-Consistent Scheme

In the Self-Consistent scheme each inclusion is assumed to be embedded in an unknown homogenised medium, so that the localization tensor \mathbb{A}_r will contain the homogenised effective stiffness tensor \mathbb{C}_{hom} . Due to the implicit form of this scheme, an iterative algorithm is required allowing the homogenised stiffness tensor to be obtained in a straightforward way. The homogenised localisation tensor, $\mathbb{A}_r^{\text{hom}}$, for the Self-Consistent Scheme is thus given as:

$$\mathbb{A}_r^{\text{hom}} = [\mathbb{I} + \mathbb{P}_{I_r}^{\text{hom}} : (\mathbb{C}_r - \mathbb{C}_{\text{hom}})]^{-1} : \left[\sum_{s=0}^N f_s [\mathbb{I} + \mathbb{P}_{I_r}^{\text{hom}} : (\mathbb{C}_s - \mathbb{C}_{\text{hom}})]^{-1} \right]^{-1} \quad (15)$$

and the homogenised effective elasticity tensor, for composites with inclusions having identical orientation and shape, is derived as:

$$\mathbb{C}_{\text{hom}} = \sum_{r=0}^N f_r \mathbb{C}_r : [\mathbb{I} + \mathbb{P}_{\text{I}_r}^{\text{hom}} : (\mathbb{C}_r - \mathbb{C}_{\text{hom}})]^{-1} \quad (16)$$

2.4 Generalized Self-Consistent Scheme

This scheme was developed on a similar basis as the SCS with the difference that the inclusion is assumed to be surrounded by some of the matrix material and subsequently embedded in the homogenised medium. The determination of the closed-form solution for this scheme is not as straightforward as in the other models, but several solutions have been proposed based on different assumptions [11, 5]. In the case of an isotropic composite material including one type of spherical inclusion, the bulk and shear moduli were obtained as:

$$\kappa_c = \frac{f_0 \kappa_0 (4\mu_0 + 3\kappa_i) + f_i \kappa_i (4\mu_0 + 3\kappa_0)}{f_0 (4\mu_0 + 3\kappa_i) + f_i (4\mu_0 + 3\kappa_0)} \quad (17)$$

where the subscripts 0, i , and c represent the matrix, inclusion and the homogenised composite, respectively. It should be noted that both GSCS and MT provide the same value for the homogenised bulk modulus. The effective shear modulus, μ_c , of the composite material can be obtained by solving the following equation:

$$A \left(\frac{\mu_c}{\mu_0} \right)^2 + B \left(\frac{\mu_c}{\mu_0} \right)^2 + C = 0 \quad (18)$$

where A , B and C are material constants which are provided in Appendix A2.

3 Material Point Method

The effect of interactions between different phases on the mechanical behaviour of a composite is assessed by using the material point method (MPM), with the benefit of simulating the detailed geometry of the REV. This method was developed in fluid dynamics and further developed by Sulsky *et.al.* [41] and extended by Sulsky and Schreyer [42] and Bardenhagen and Kober [3] among others to model solid mechanics problems. Technically, the MPM is a meshless method in which

the material points **that also** possess the state variables (position, mass, velocity, acceleration, stress state, etc), are Lagrangian and represent the discretised continuum. They are independent of the Eulerian fixed computational mesh. Since the method uses an arbitrary mesh, distortion inherent from the usual Lagrangian formulations is avoided. Conservation of mass is automatically satisfied as the mass of each point is kept constant during the calculation. At each time step, the information is initially extrapolated from the material points to the mesh, where the governing equations are solved and the solutions transferred back to the mesh and updated [46,21]. Figure 2 shows how the particles, in a Lagrangian formulation move through the Eulerian mesh.

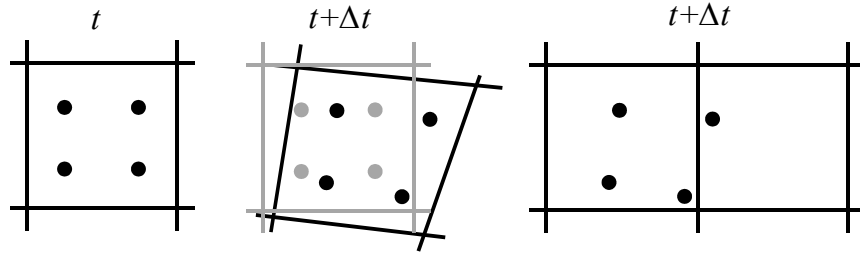


Fig. 2 Description of a continuum using MPM.

Assuming that the particle quantities such as position, mass, external force, volume, velocity, stress and strain $\{\mathbf{x}_p^t, M_p, \mathbf{f}_p^t, V_p^t, \mathbf{v}_p^t, \boldsymbol{\sigma}_p^t, \boldsymbol{\varepsilon}_p^t\}$, have been obtained (initialised) at time t , the nodal values for mass and momentum can be obtained as:

$$m_n^t = \sum_{i=1}^p N_n(\mathbf{x}_i^t) M_i; \quad m_n^t \mathbf{v}_n^t = \sum_{i=1}^p N_n(\mathbf{x}_i^t) M_i \mathbf{v}_i^t \quad (19)$$

where N is the conventional finite element shape function and p is the total number of material points inside the element.

The nodal external and internal forces follow straightforwardly as

$$\mathbf{f}_n^{ext,t} = \sum_{i=1}^p N_n(\mathbf{x}_p^t) \mathbf{f}_p^t; \quad \mathbf{f}_n^{int,t} = - \sum_{i=1}^p V_p^t \boldsymbol{\sigma}_p^t \nabla N_n(\mathbf{x}_p^t) \quad (20)$$

where ΔN is the first derivative of the shape function.

The total nodal forces $\mathbf{f}_n^{tot,t} = \mathbf{f}_n^{ext,t} + \mathbf{f}_n^{int,t}$ and nodal momentum are subsequently used in conjunction with the widely used explicit Euler forward time scheme. The velocities and positions of the particle at time $t + \Delta t$ are updated as follows:

$$\mathbf{v}_p^{t+\Delta t} = \mathbf{v}_p^t + \Delta t \sum_n N_n(\mathbf{x}_p^t) \mathbf{f}_n^t / m_n^t \quad (21)$$

and positions

$$\mathbf{x}_p^{t+\Delta t} = \mathbf{x}_p^t + \Delta t \sum_n N_n(\mathbf{x}_p^t) (\mathbf{m}\mathbf{v})_n^t / m_n^t \quad (22)$$

In view of Equation (21), the velocity gradient of the particles can be further re-written as:

$$\mathbf{L}_p^{t+\Delta t} = \nabla \mathbf{v}_p^{t+\Delta t} = \sum_n \nabla N_n(\mathbf{x}_p^t) \mathbf{v}_n^{t+\Delta t} \quad (23)$$

and the corresponding deformation gradients operators of the finite strain situations can be directly obtained as:

$$\mathbf{F}_p^{t+\Delta t} = (\mathbf{I} + \mathbf{L}_p^{t+\Delta t} \Delta t) \mathbf{F}_p^t \quad (24)$$

and the volume changes are updated at the particle level according to:

$$V_p^{t+\Delta t} = \det(\mathbf{F}_p^{t+\Delta t}) V_p^0 \quad (25)$$

To account for large strain condition, the Jaumann stress rate is used to update particle stresses as follows:

$$\boldsymbol{\sigma}_p^{t+\Delta t} = \boldsymbol{\sigma}_p^t + (\boldsymbol{\sigma}_p^t \boldsymbol{\omega}_p^{t+\Delta t} - \boldsymbol{\omega}_p^{t+\Delta t} \boldsymbol{\sigma}_p^t) + \mathbb{C}_r : \Delta \boldsymbol{\varepsilon}_p^{t+\Delta t} \quad (26)$$

$$\Delta \boldsymbol{\varepsilon}_p^{t+\Delta t} = \frac{\Delta t}{2} (\mathbf{L}_p^{t+\Delta t} + (\mathbf{L}_p^{t+\Delta t})^T) \quad (27)$$

$$\boldsymbol{\omega}_p^{t+\Delta t} = \frac{\Delta t}{2} (\mathbf{L}_p^{t+\Delta t} - (\mathbf{L}_p^{t+\Delta t})^T) \quad (28)$$

where $\Delta \boldsymbol{\varepsilon}_p$ is the incremental linear strain, $\boldsymbol{\omega}_p$ is the rotation matrix and \mathbb{C}_r is the stiffness tensor for the phase which is assigned to the material point.

Practical implementation of MPM involves more computational issues. For example, explicit nature of the presented MPM formulation only allows for adoption of linear elements; however, the first derivative of shape functions for these elements are discontinuous which can lead to numerical noise in the calculation known

as particle crossing problem [3]. Several improvements including using Generalized Interpolation [1], Spline shape function [2], anti-locking approach [25, 26] and mixed integration [6] were proposed to treat such problem. Here, the computationally efficient method of mixed integration was implemented. In this approach, an element located inside the continuum body is assumed to be fully filled with material points. The state variables are mapped from its material points to the Gauss points and the integration is carried out in a similar fashion to the conventional finite element method. However, for an element located around the boundaries of the continuum body, the conventional MPM integration over the material points is carried out when the total volume of the material points inside that element is less than a fraction of the element volume, usually between 0.8 and 0.9. Otherwise, the element integration is performed similarly to the fully-filled elements. It should be noted that this approach is only valid for quasi-static simulations. For more details on the formulation and implementation of this method the reader is referred to [6, 21].

4 Matrix-inclusion morphology

Scanning Electron Microscope (SEM) images of shale samples can provide important insights into their microstructure. Figure 3 shows a SEM image on a shale cut perpendicular to the bedding plane. It can be seen that, at the scale of a few micrometres, shales can be described as composite materials in which the inclusions are surrounded by the matrix phase. These inclusions are characterised by various shapes ranging from spherical to angular and including highly irregular shapes for which the orientation is not clearly defined.

Here, the MPM is used to simulate the mechanical behaviour of shale with different microstructures. The numerical results are then compared with the homogenisation schemes described in the previous section in order to evaluate the modelling capabilities of the mean-field methods in predicting the homogenised behaviour of highly complex natural composites such as clayey rocks. We extend previous studies by considering angular inclusion shapes, highly-contrasting matrix and inclusion properties, high concentrations of inclusions, three phase composites with complex random micro-structures. A summary of typical values of elastic proper-

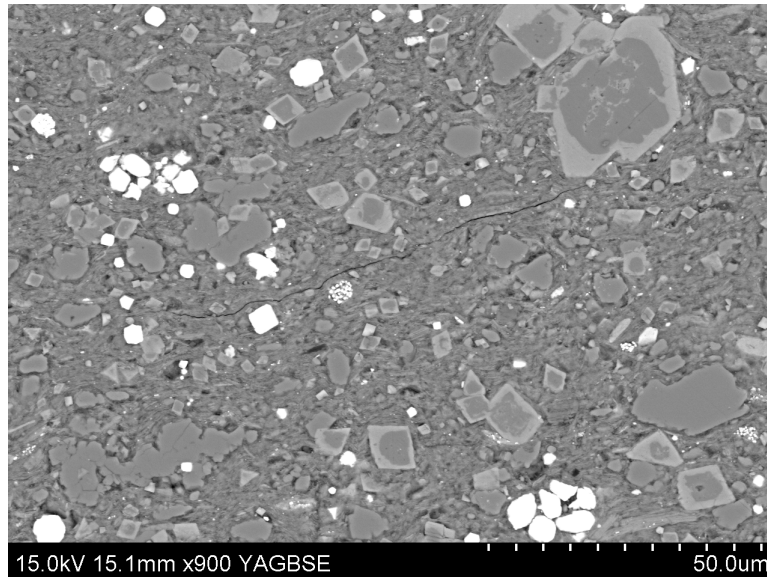


Fig. 3 Typical SEM image of a shale sample from a cutting section perpendicular to bedding plane.

ties of common mineral inclusions in shale rocks are given in Table 1. Additionally, the following material properties are assigned to the isotropic porous clay matrix: Young's modulus $E = 3$ GPa Poisson's ratio $\nu = 0.3$ [15].

Table 1 Elastic properties of some common inclusions found in clayey rocks.

| Mineral | Young's modulus (GPa) | Poisson's ratio | Indentation modulus $E/(1 - \nu^2)$ (GPa) | Source |
|-----------|--------------------------|-----------------|---|--------------------------------|
| Calcite | 95 | 0.27 | — | Guery <i>et al.</i> [15] |
| Quartz | 101 | 0.06 | — | Guery <i>et al.</i> [15] |
| Pyrite | 265.38 | 0.18 | — | Whitaker <i>et al.</i> [45] |
| Feldspars | 75.93 | 0.22 | — | Bass [4] |
| Kerogen | — | — | 10.5 | Zeszotarski <i>et al.</i> [48] |

4.1 Composite with single inclusion

The analytical solutions for the mean-field homogenisation methods were developed on the basis of a single inclusion with a spherical or elliptical shape, embedded in the matrix phase [49]. Such assumptions do not recognize the natural shape of inclusions in clayey rocks that are mostly small, angular pieces of hard minerals such as calcite and quartz. In order to evaluate such analytical solutions and account for the angularity of real inclusions, it is proposed to explore the simulations of a single inclusion with a spherical or cubic shape. Due to the symmetry of the problem under consideration, only one quarter of the REV model with appropriate

boundary conditions is simulated (Figure 4). Two different loading conditions are performed by controlling the displacements. In the first loading, a uniform normal displacement has been applied at the top and two perpendicular lateral boundaries of the REV model, with normal movements not permitted at the remaining boundaries. This loading condition is expected to generate hydrostatic compression and can be used to estimate the bulk modulus of the REV. In the second loading, a uniaxial compression is simulated by imposing the vertical displacement at the top boundary of the REV and fixing the vertical movement at the opposite boundary. This test was undertaken to estimate the Young's modulus of the REV.

In addition, an arrangement of eight material points per element, with 8000 points in total number, was determined through a mesh sensitivity analysis carried out to minimise the discretisation error and improve the accuracy of the results. This mesh, together with the described loading and boundary conditions, has been adopted in all simulations unless otherwise mentioned.

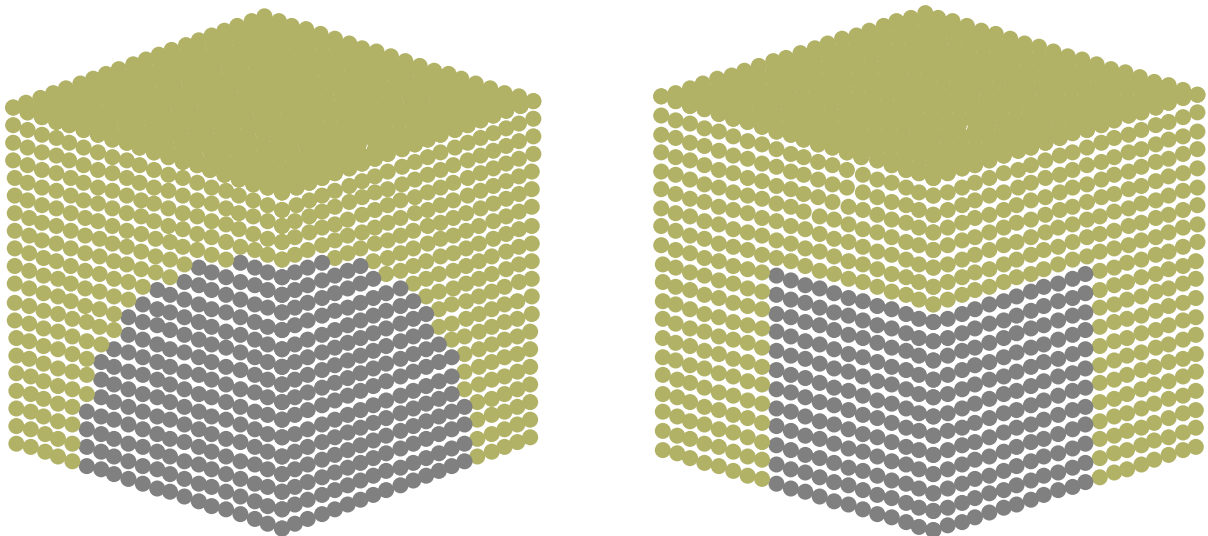


Fig. 4 MPM models of the spherical and cubic inclusions embedded in a matrix

Figure 5 shows a comparison of the normalised bulk modulus for single spherical and cubic inclusions and the values predicted by the different homogenisation methods, for different volume fractions of the inclusion. The comparison between the simulated and calculated bulk modulus using the MT and GSCS models are in good agreement. However, for the SCS, it can be seen that a stiffer behaviour is predicted for a volume fraction of the inclusion greater than approximately 20%,

which results in an overestimation of the bulk modulus. The analyses also indicate that there is no influence of the cubic-shaped inclusion on the homogenised bulk modulus of the REV.

Comparison of the simulated and calculated normalised Young's modulus is also shown in Figure 5. Overall, the numerical results are in good agreement with the SCS, up to volume fractions of inclusion around 42%. For inclusion concentrations above this threshold, the SCS overestimates the Young's modulus. Both MT and GSCS predictions slightly underestimate the Young's modulus and the prediction error increases with increasing inclusion volume fraction. It should be noted that the MT and GSCS models predict virtually identical moduli. However, due to the simplicity of the implementation of MT compared to the GSCS scheme, this scheme allows a variety of clayey rocks to be investigated, for example with a transversely isotropic matrix, a multi-phase composite and with different inclusion shapes. In addition, as the inclusion volume fraction increases above 20%, there is an underestimation of the effective properties using the DS model, leading to a softer response. This is due to the concentration of inclusions and their interaction, which are not accounted for in the formulation of DS.

4.2 Composite with Randomly Distributed Inclusions

Shales are very complex multi-phase composite materials which usually contain various types of inclusions such as calcite, quartz, pyrite, feldspar, kerogen, etc. Calcite and quartz constitute the highest volume fractions of inclusions, with other minerals usually less than 15% [27, 33, 39]. In addition, there is a significant strength difference between the major inclusions (calcite/quartz) and the low volume fraction inclusions. For example, pyrite is almost three times stiffer than calcite whereas kerogen is considered as a very soft substance (see Table 1).

For the final investigation of the predicted results by homogenisation techniques, they are evaluated for the case of a composite with randomly distributed grains which is more close to the real microstructure of shales. To increase the level of complexity, two types of cubic inclusions with different sizes including calcite and pyrite are considered. The ratio of inclusions volumes to the total volume of REV are 0.33 and 0.1 for calcite and pyrite grains, respectively. **The model consists of**

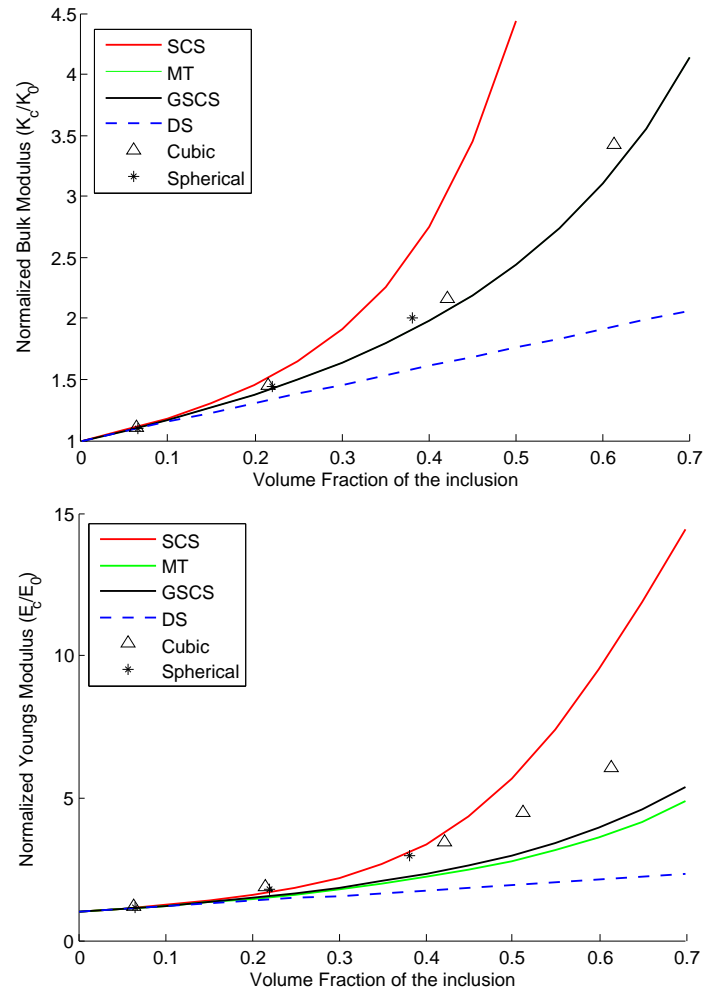


Fig. 5 Comparison between the results of numerical and mean-field homogenisation methods for normalized bulk and Young's moduli of the models with various volume fractions of spherical and cubic inclusions.

18000 material points with eight points per element (Figure 6). The inclusions are randomly placed in the matrix in such way that they are not in contact with each other and all of them are surrounded by at least one layer of material points having the clay matrix properties.

Three random models were generated and both hydrostatic and uniaxial compression tests were carried out. The bulk modulus, Young's modulus and two components of the stiffness tensor obtained from numerical simulation and two homogenisation schemes are presented in Table 2. Based on the results, MT provides a very good prediction for bulk modulus and a fair prediction for Young's modulus. In addition, although the error of prediction for Young's modulus using SCS is a little less than MT at this volume fraction of inclusions, the bulk modulus is overestimated. In fact, the results are in agreement with the trend being observed for the case of a single inclusion. Considering the results obtained for stiffness tensor com-

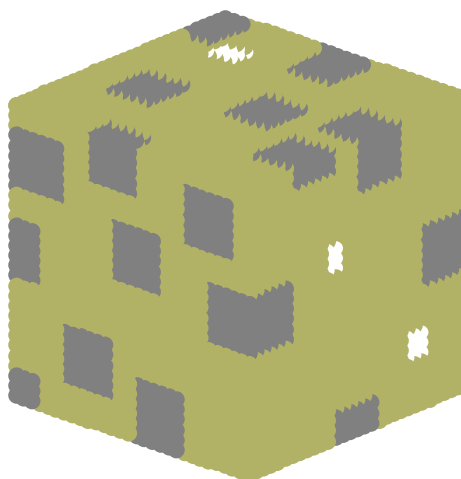


Fig. 6 A REV with randomly distributed calcite (black) and pyrite (white) grains; volume fractions are 33% and 1%, respectively.

ponents, no clear advantage can be observed between using MT or SCS to predict the overall, homogenised stiffness tensor. This is because for an isotropic material, each component of its stiffness tensor is a function of two elastic constants which combine the errors obtained for bulk and Young's moduli.

Table 2 Numerical and mean-field methods results for the random three-phase composite.

| Normalized Modulus | | K_c/K_0 | E_c/E_0 | C_{11}^c/C_{11}^0 | C_{12}^c/C_{12}^0 |
|--------------------|------------|-----------|-----------|---------------------|---------------------|
| Method | Simulation | 1.86 | 2.34 | 2.83 | 2.16 |
| | MT | 1.77 | 1.97 | 2.142 | 1.91 |
| | SCS | 2.38 | 2.66 | 2.91 | 2.57 |

Theoretically, the mean-field methods were formulated for N different phases, which make it possible to study composites with various inclusions. On the other hand, from a practical point of view, it can be difficult to accurately determine the volume fraction of each inclusion, especially when its concentration is very low or has a similar density as the other inclusions. Mineralogical information may be supplied simply as the volume fraction of clay and non-clay minerals. It is therefore of interest to quantify the effect of ignoring low concentrated minerals and simplifying the shale to two-phase composite on its homogenised response.

Here, a simple example which consists of a small pyrite inclusion placed within calcite grains has been adopted to study the difference in the homogenised response between a real composite and a simplified one. The volume fraction of pyrite is selected based on common values found in shale samples for minor inclusions. For example, the Kimmeridge shale consists of 30.5% quartz, 2.1% pyrite, 7.2%

feldspar and the rest form different clay minerals [19]. A model with 26.8% calcite and 11.3% pyrite is generated. The results of the normalized elastic moduli for the three-phase composite and the simplified one in which all the clay minerals are assumed to be quartz are presented in Table 3, indicating that the lack of information about these low concentration minerals may not affect the results significantly. It can also be observed that the SCS is more sensitivity to this simplification than MT method. Generally, it can be summarized that this practical simplification appears to be acceptable.

Table 3 Numerical and mean-field methods results for both three-phase and simplified composite.

| Model | | Three-Phase Comp. | | Simplified Comp. | |
|--------------------|------------|-------------------|-----------|------------------|-----------|
| Normalized Modulus | | K_c/K_0 | E_c/E_0 | K_c/K_0 | E_c/E_0 |
| Method | Simulation | 1.99 | 2.33 | 1.98 | 2.32 |
| | MT | 1.94 | 2.17 | 1.92 | 2.15 |
| | SCS | 2.68 | 3.31 | 2.60 | 3.16 |

5 Porous clay matrix

One of the complexities of clayey rocks is that the matrix itself is a porous material for which the mechanical properties of its solid unit (clay minerals) are poorly constrained. Nevertheless, the mechanical properties of the solid clay, in conjunction with the total porosity of the clay matrix, play a major role in the overall macroscopic mechanical response of clayey rocks. Due to the difference in length-scale between void and porous clay matrix, the homogenisation schemes can be adapted to account for the effects of porosity on the mechanical response of the matrix and to back-analyse the solid clay properties. In this section, the accuracy and capabilities of the homogenisation methods for predicting the mechanical response of porous composites are investigated. According to the experimental data available in the literature, the porosity of clay matrix in shales varies between 2 to 40% [27, 33, 39]. Moreover, determination of the elastic properties of solid unit of clay is still an open topic, which is out of the scope of this research, with different values obtained by different researchers. Here, values of 5 GPa for Young's modulus (E) and 0.33 for Poisson's ratio (ν) were adopted for the solid unit of clay [37].

5.1 Simplified porous matrix micro-structure

As the real microstructure of the porous clay matrix is difficult to characterise accurately, two different idealized models are considered for the arrangement of voids and clay particles. In the first model, it is assumed that the voids are embedded in solid clay, similar to the matrix-inclusion placement; in the second model, the solid unit of clay is considered to be spherical particles in contact with each other and forming a network of connected pores (Figure 7). Both models are subject to hydrostatic loading with different porosities.



Fig. 7 MPM models for isolated void (left) and connected pore network (right). The black particles are deleted to generate voids.

The results of the normalized bulk moduli are plotted in Figure 8 along with the predicted moduli by the mean-field homogenisation schemes. The MT method is able to predict the effective bulk modulus for a porosity ranging between 0 and 1. In contrast, the SCS prediction of the same effective modulus is only valid up to porosity values around 0.5, after which the stiffness reaches non-physical values. The same observation can be made for the DS model, for which non-physical values are predicted for porosities above 0.33. In addition, from Figure 8 it can be concluded that the stiffness response of the first model with isolated voids is in good agreement with the MT results. In contrast, the second model, with a pore network, shows a good agreement with the SCS predictions.

Published results of indentation tests and imaging techniques along with theoretical concepts in granular media are next used to elucidate which of the two modelled arrangements might be more realistic to represent the clay matrix microstructure. In work undertaken by Ulm and Abousleiman [43] on different shale samples, nanoin-

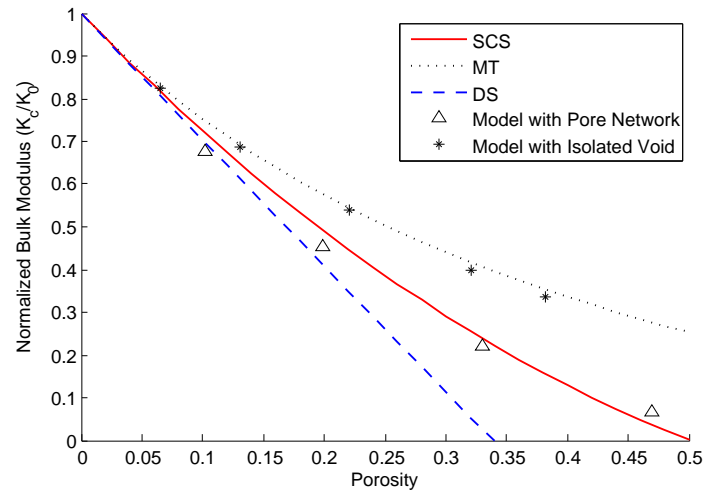


Fig. 8 Comparison between the results of numerical and homogenisation methods for normalized bulk modulus of a clay matrix with isolated (crosses) and connected (triangles) pores.

dentation tests highlighted the linear relationship between the indentation modulus of clay matrix and porosity, with the indentation moduli reaching the value of zero when the porosity approached a value of approximately 0.5 (Figure 9). Additionally, in the model with spherical clay particles and pore network (see Figure 7), if the radius of particles is decreased until the porosity reaches a value of approximately 0.52, then the contact between the particles is completely lost. This value is almost equal to the one observed by Onoda and Liniger [32] for the highest possible porosity in the case of granular packing of having uniform spheroids.

The relationship between SCS-predicted, normalized bulk modulus and porosity is almost linear and predicts that the stiffness becomes zero when the porosity is 0.5 (Figure 8). It therefore appears that the SCS is an appropriate model with which to homogenize a porous clay matrix, as its results are well matched with both theoretical results and experimental observations.

5.2 Porous Matrix with Random pores

Having evaluated the performance of the homogenisation methods with simplified pore systems, a realistic 3D stochastic pore network model obtained from high resolution SEM images of a shale rock [23] has also been simulated. The stochastic model consists of a cube with 200 voxels in each dimension, with a property of either a pore or solid assigned to each voxel. Three smaller cubes with 25 voxels in each dimension having different porosities were selected from inside the stochas-

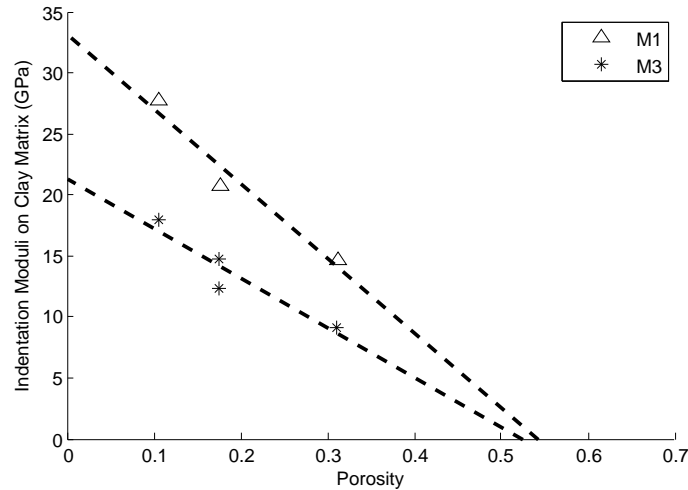


Fig. 9 Indentation moduli parallel (M_3) and perpendicular (M_1) to bedding plane of shale samples versus the porosity (Modified from Ulm and Abousleiman [43]).

tic model (Figure 10). The three stochastic samples used in the simulations, are generated by mapping each voxel into one element.

Figure 11 shows the averaged normalized Young's moduli in three directions obtained from numerical simulations. A good agreement can be observed between numerical results and values predicted by SCS model.

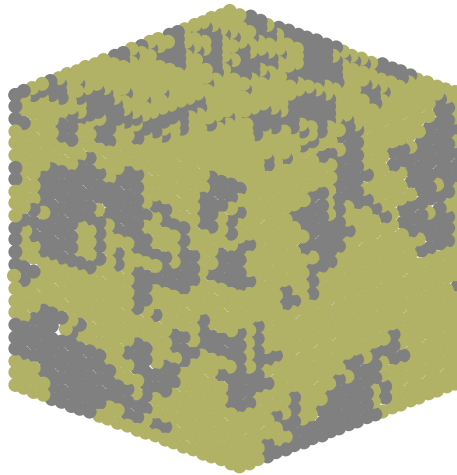


Fig. 10 Stochastic model of porous clay matrix with porosity of 0.32 (pores are represented by grey particles).

It is also well-known that the shale pore system is complex, consisting of both connected and isolated pores ranging in size from a nanometre to a few micrometres [8, 10, 31]. Consequently, the stochastic models seem to represent the experimental observations on both microstructure and the mechanical response of porous clay.

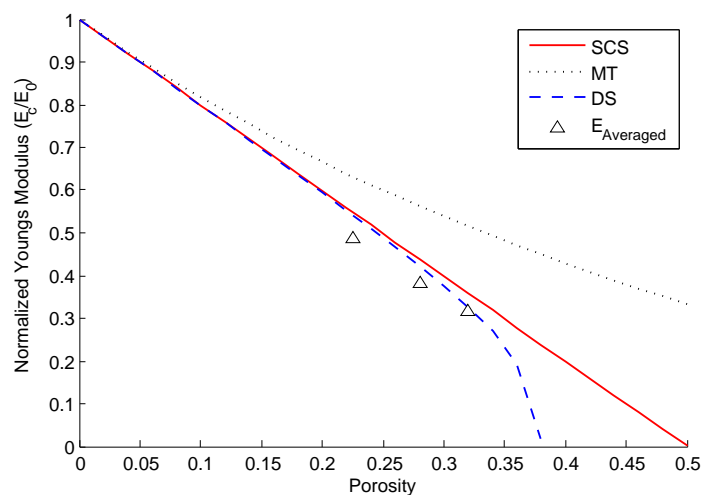


Fig. 11 Comparison between numerical and mean-field homogenisation methods results of normalized averaged Young's modulus in three directions for the stochastic models.

To further study the mechanical response of these random pore systems, a REV was considered in which the porosity was randomly distributed through the model. As there was no restriction on the placement of the pores, a matrix with both isolated and connected pores was formed (Figure 12). Three different target porosities below and above the threshold of 50% of porosity were considered and six random models were generated for each target porosity.

Figure 13 shows the numerical predictions of the effective bulk and Young's moduli along with the results obtained from the adopted homogenisation schemes. It can be seen that for the case of a composite with random porosity below 50%, the SCS provides good predictions compared to the other schemes. It is also observed that when the porosity exceeds the threshold of 50%, the stiffness converges towards a value of zero. Additionally, the three different random models for each target porosity produce approximately the same mechanical behaviour which makes these results reproducible with no noticeable anisotropy induced by the pore network.

Since the microstructure of a porous clay matrix is difficult to characterise, conceptual models of porous clay matrix offer an efficient quantification of its mechanical response. This allows the overall elastic-plastic behaviour of the clayey rocks to be investigated. When pore spaces embedded in solid clay are assumed to be spherical and isolated, closed-form solutions for the homogenised elastic-plastic response

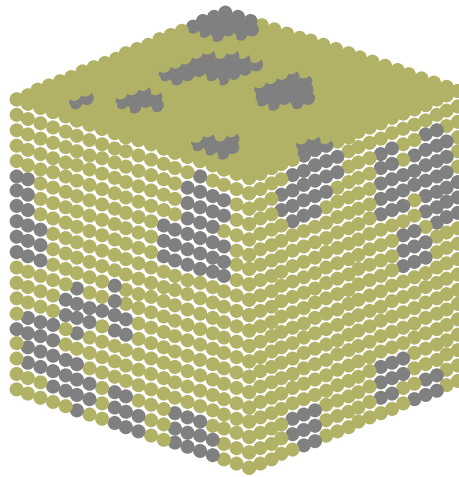


Fig. 12 REV for a matrix with porosity of 0.3 and a random distribution of pores (pores are represented by black particles).

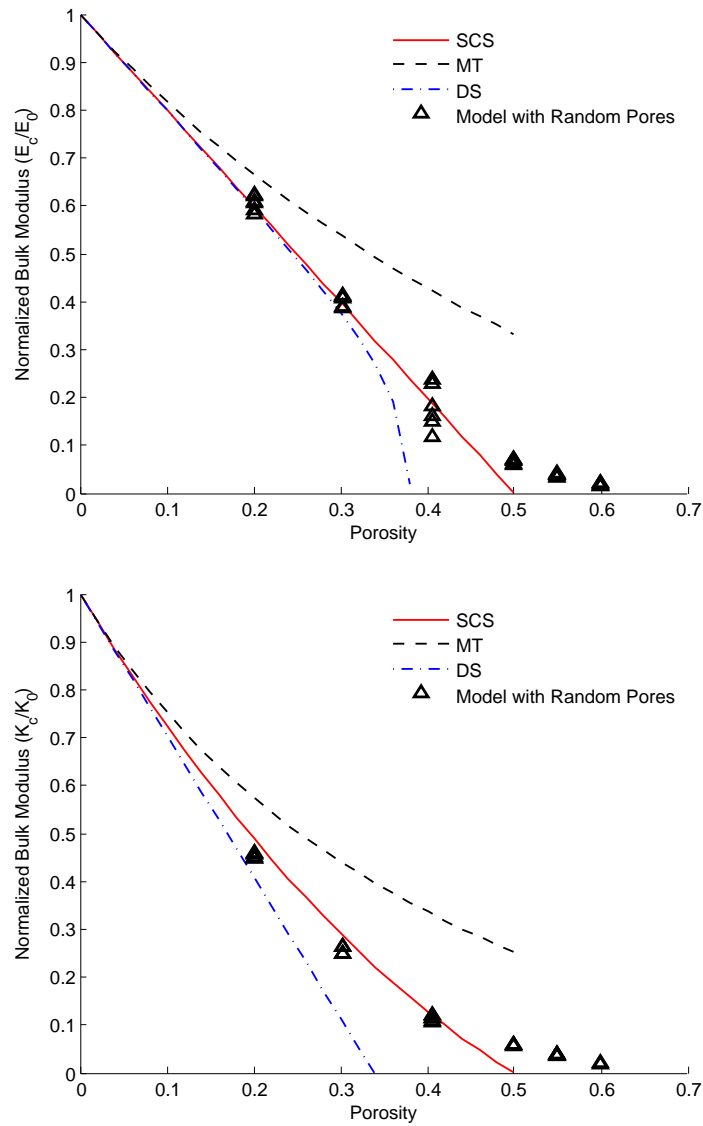


Fig. 13 Comparison between numerical and mean-field methods results of normalized bulk and Young's moduli for the model with random porosity.

can be derived [24,37,38]. However, the choice of simplified, isolated voids in this study, resulted in a poor prediction of the mechanical response of porous clay.

Using models which assume random pores in a porous clay matrix, the mechanical response is more consistent with the theoretical and experimental results. In addition, the generation of different random pores system to capture a given target porosity would not alter the overall mechanical response. The approach followed here may produce more accurate results when a transversely isotropic elastic response along with a suitable failure surface such as Drucker-Prager are considered for the solid unit of clay.

6 Homogenisation of shale rock elastic response

Shale rocks, in general, are transversely isotropic (TI) in elastic response and it is well known that this property originates from aligned plate-like clay minerals within the shale [34]. However, different models have been proposed to explain this TI response. For example, Hornby et al. [18] assumed that the shale matrix consists of elliptical pores and elliptical isotropic elastic clay particles, and these elementary building blocks are the source of anisotropy. This idea has been adopted in some of the subsequent studies [20,50,44]. Ortega et al. [33], on the other hand, implicitly considered the effect of the plate-like elements by a TI set of elastic constants for the solid unit of the matrix.

In this section, homogenisation formulations are used to predict experimental measurements of the elastic properties of shale core samples. Shales with different inclusion volume fractions were selected to show how understanding of the performance of each mean-field homogenisation formulation could help to better interpret the predictive results.

In previous sections, it was shown that SCS is a suitable method to homogenise the elastic response of the clay porous matrix. However, the overall elastic properties of matrix-inclusion morphology follows the described formulations up to a certain level of inclusion concentration. Here, the TI properties of solid clay determined by Ortega et al. [33] is adopted in conjunction with shale characterisations, porosity and mineralogical data, for three shale samples to predict their macroscopic elastic constants. SCS is selected for the first level of homogenisation of the

porous clay, and the matrix-inclusion is upscaled using both MT and SCS. Table 4 contains the shales' characterisations which are required to homogenise their mechanical response. In addition, Eq. 29 provides the adopted five elastic constants of TI solid clay in which axis 3 is the axis of symmetry for a TI medium. The inclusion properties can also be found in Table 1. The porosity (ϕ) is assumed to be entirely in the shale matrix which is the porous clay in these samples. Thus, the measured shale porosity (ϕ_{shale}) provided in the references should be converted to the porosity of the clay matrix as $\phi_{clay} = \phi_{shale}/f_{matrix}$ in order to be considered in the first level of homogenisation. It should be noted that the overall elastic response is now TI which requires the appropriate Hill's tensor (\mathbb{P}_T^0). For the explicit formulae of the components of this tensor for a spherical inclusion embedded in a transversely isotropic matrix, readers are referred to Fritsch and Hellmich [13].

Table 4 Shale samples characterisation (Extracted from Hornby [19] and Domnesteau et al. [12])

| Sample | Kimmeridge Shale | Jurassic Shale | Domnesteau et al. |
|-------------------------------------|---------------------|----------------|-------------------|
| Mineralogical Data | Volume fraction (%) | | |
| Quartz | 30.5 | 31 | 44.4 |
| Calcite | — | 2 | — |
| Pyrite | 2.1 | 5 | 1.5 |
| Feldspar | 7.2 | 4 | 6.5 |
| Porous clay (f_{matrix}) | 60.2 | 58 | 47.6 |
| Sum of inclusions (f_{Inc}) | 39.8 | 42 | 52.4 |
| Shale porosity (ϕ_{shale}) | 2.5 | 10.5 | 14 |
| Matrix porosity (ϕ_{matrix}) | 4.15 | 18.1 | 29.4 |

$$\begin{aligned}
 C_{11} &= 44.9; & C_{33} &= 24.2; & C_{13} &= 18.1; \\
 C_{44} &= 3.7; & C_{66} &= 0.5(C_{11} - C_{12}) = 11.6
 \end{aligned}
 \tag{29}$$

Here, the predicted values for two elastic constants of C_{11} and C_{33} which are respectively related to directions parallel and perpendicular to bedding, are compared with the experimental measurements (Figure 14). It can be concluded that the predicted values of SCS are comparable with the experimental results for Kimmeridge and Jurassic shales but do not perform well for the sample from Domnesteau et al. [12]. In order to understand this prediction error, we need to refer back to Figure 4 and 5 where the basic problem of a single inclusion was considered. It was illustrated that for an inclusion concentration above 42 % neither SCS nor MT can provide a good prediction of matrix-inclusion morphology. The third shale sam-

ple contains around 53 % inclusion which is higher than the applicability of these formulations. The elastic properties of this shale should lie between the predicted values of SCS and MT. Figure 14 clearly shows the elastic properties are underestimated or overestimated by the MT and SCS, respectively. On the whole, the key to successful and reliable implementation of homogenisation formulations is to fully understand their limitations, range of applicability and representative microstructure.

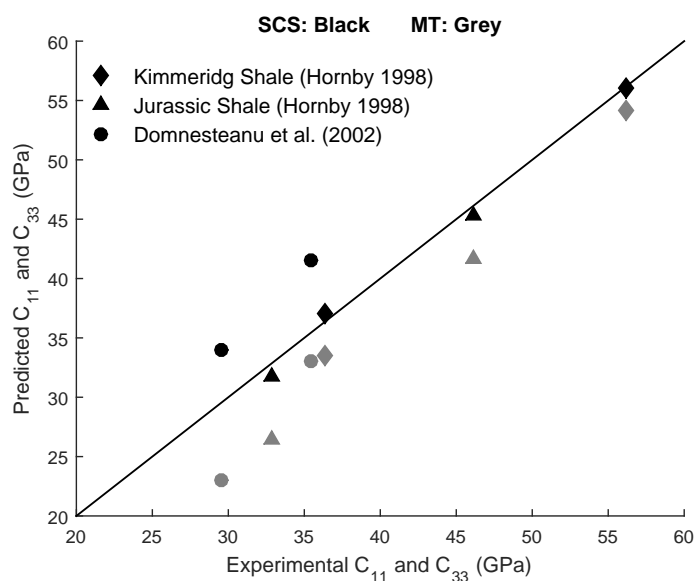


Fig. 14 Experimental results versus predicted values for elastic response of three shale samples with SCS at the first level and both SCS and MT at the second level of homogenisation.

7 Conclusion

A comparative evaluation study of the macroscopic elastic response of clayey rocks using different homogenisation schemes and numerical simulations that account for microstructures has been carried out. Clayey rocks were considered to be two-level composites consisting of solid clay with pores at the first level and a porous matrix with solid mineral inclusions at the second level.

The simulation results of matrix-inclusion morphology presented here reveal that MT and GSCS homogenisation schemes provide the most accurate predictions of the homogenised bulk modulus; the SCS model overestimated the bulk modulus, particularly when the volume fraction of inclusions is high. In contrast, the Young's modulus is better predicted by the SCS model, for materials with up to 42% vol-

ume fraction of inclusions. Consequently, no clear advantage was offered by either scheme in predicting the homogenised stiffness matrix, for which all the components are functions of the two elastic constants, i.e. the bulk and shear moduli.

Two different microstructures for the porous clay matrix were considered, one consisting of isolated pores and a second with a connected pore network. For a system with isolated pores, the MT model more accurately reproduces the macroscopic response, whilst the SCS model is more effective for a matrix with a pore network. In addition, pore networks for shales with (a) randomly distributed pores and (b) stochastically-developed pore networks using SEM images have been simulated and the results compared with those obtained using homogenisation techniques. In both cases, the SCS model gives the best prediction of the macroscopic rock stiffness response, with an almost linear porosity-stiffness relationship up to 50% porosity, similar to experimental studies on the mechanical response of the clay matrix in shales .

These results, along with the experimental data which suggest that most pores in shales are connected, show that the SCS is the most appropriate model with which to homogenize the elastic properties of a porous clay matrix. Importantly, the conceptual, randomly distributed pore system could be adopted as a model for clay matrix with which to study the macroscopic elastic-plastic response and flow properties of fine-grained sedimentary rocks dominated by a porous clay matrix.

Finally, the homogenisation techniques were used to predict experimental measurements of shale elastic response of three well-characterised shales with different porosities and inclusion volume fractions covering a wide range of microstructure. A numerical experiment has been performed, and the results confirm the suitability of the method to capture the response of real complex microstructure of shales. This reveals the importance of undertaking numerical studies when assessing the applicability and limitations of homogenisation techniques.

Acknowledgements: The authors would like to thank Dr. Jingsheng Ma for providing the stochastic model for porous clay. We also thank Mr. Leon Bowen for his help with SEM imaging of several shale samples.

References

1. Andersen, S., Andersen L.: Modelling of landslides with the material-point method. *Comput. Geosci.* **14**,137-147 (2010). DOI: 10.1007/s10596-009-9137-y
2. Andersen, S., Andersen L.: Analysis of spatial interpolation in the material-point method. *Computers and Structures.* **88**, 506-518 (2010). DOI:10.1016/j.compstruc.2010.01.004
3. Bardenhagen, SG., Kober, E.M.: The generalized interpolation material point method. *Computer Modeling in Engineering and Sciences*, **5**(6), 477495 (2004).
4. Bass, J.D.: Mineral Physics and Crystallography; In: A Handbook of Physical Constants, Ahrens T J (ed.), AGU Reference Shelf (1995).
5. Benveniste, Y.: Revisiting the generalized Self-Consistent Scheme in composites: clarification of some aspects and a new formulation. *Journal of the Mechanics and Physics of Solids.* **56**, 2984-3002 (2008).
6. Beuth, L., Wiecekowsk, Z., Vermeer, P.A.: Solution of quasi-static large-strain problems by the material point method. *Int. J. Numer. Anal. Meth. Geomech.* **35**, 1451-1465 (2011). DOI: 10.1002/nag.965
7. Bobko, C., Ulm, F.J.: The nano-mechanical morphology of shale. *Mechanics of Materials.* **40**, 318-337 (2008). doi:10.1016/j.mechmat.2007.09.006
8. Chalmers, G.R., Bustin, R.M., Power, I.M.: Characterization of gas shale pore systems by porosimetry, pycnometry, surface area, and field emission scanning electron microscopy/transmission electron microscopy image analyses: Examples from the Barnett, Woodford, Haynesville, Marcellus, and Doig units. *The American Association of Petroleum Geologists (AAPG) Bulletin.* **96**(6), 1099-1119 (2012).
9. Chateau, X., Dormieux, L.: Micromechanics of saturated and unsaturated porous media. *International Journal of Numerical and Analytical Methods in Geomechanics.* **26**, 831-844 (2002). DOI: 10.1002/nag.227
10. Chen, L., Zhang, L., Kang, Q., Viswanathan, H.S., Yao, J., Tao, W.: Nanoscale simulation of shale transport properties using the lattice Boltzmann method: permeability and diffusivity. *Scientific Reports.* **5**(8089) (2015). DOI: 10.1038/srep08089
11. Christensen, R.M., Lo, K.H.: Solutions for effective and shear properties in three phase and cylinder models. *Journal of the Mechanics and Physics of Solids.* **27**, 315-330 (1979).
12. Domnesteau, P., McCann, C., Sothcott, J.: Velocity anisotropy and attenuation of shale in under- and overpressured conditions. *Geophys Prosp* **50**, 487503 (2002).
13. Fritsch, A. Hellmich, C.: Universal microstructural patterns in cortical and trabecular, extracellular and extravascular bone materials: Micromechanics-based prediction of anisotropic elasticity. *Journal of Theoretical Biology* **224**, 597620 (2007). DOI:10.1016/j.jtbi.2006.09.013
14. Guery, A.A., Cormery, F., Shao, F., Kondo, D.: A micromechanical model of elastoplastic and damage behavior of a cohesive geomaterial. *Computers and Geotechnics. International Journal of Solids and Structures.* **45**, 1406-1429 (2008).
15. Guery, A.A., Cormery, F., Shao, F., Kondo, D.: A comparative micromechanical analysis of the effective properties of a geomaterial: Effect of mineralogical compositions. *Computers and Geotechnics.* **37**, 585-593 (2010). DOI: 10.1016/j.compgeo.2010.02.008
16. Hbaieb, K., Wang, Q.X., Chia, Y.H.J., Cotterell, B.: Modelling stiffness of polymer/clay nanocomposites. *Polymer.* **48**, 901-909 (2007).
17. Hill, R.: A self-consistent mechanics of composite materials, *Journal of Mechanics and Physics of Solids*, **13**, 213-222 (1965).
18. Hornby, B.E., Schwartz, L., Hudson, J.: Anisotropic effective medium modeling of the elastic properties of shales. *Geophysics*, **59**, 1570-83 (1994).
19. Hornby B.E.: Experimental laboratory determination of the dynamic elastic properties of wet, drained shales. *Journal of Geophysical Research*, **103**(B12), 29945-29964 (1998).
20. Jakobsen, M., Hudson, J.A., Johansen, T.A.: T-matrix approach to shale acoustics. *Geophysical Journal International*, **154**, 533558 (2003).
21. Jassim, I., Stolle, D., Vermeer, P.: Two-phase dynamic analysis by material point method. *Int. J. Numer. Anal. Meth. Geomech.* (2012). DOI: 10.1002/nag.2146
22. Klusemann, B., Svendsen, B.: Homogenisation methods for multi-phase elastic composites: Comparisons and benchmarks. *Technische Mechanik.* **30**(4): 374-386 (2010).
23. Ma, J., Sanchez J.P., Wu K., Couples G.D., Jiang Z.: A pore network model for simulating non-ideal gas flow in micro- and nano-porous materials. *Fuel*, **116**, 498-508 (2014). <http://dx.doi.org/10.1016/j.fuel.2013.08.041>
24. Maghous, S., Dormieux, L., Barthelemy, J.F.: Micromechanical approach to the strength properties of frictional geomaterials. *European Journal of Mechanics A/Solids* **28**, 179-188 (2009). doi:10.1016/j.euromechsol.2008.03.002
25. Mast, C.M., Mackenzie-Helnwein P., Arduino, P., Miller, G.R., Shin W.: Mitigating kinematic locking in the material point method. *Journal of Computational Physics*, **231**, 5351-5373 (2012).
26. Mast, C.M., Arduino, P., Miller, G.R., Shin W., Mackenzie-Helnwein P.: Avalanche and landslide simulation using the material point method: flow dynamics and force interaction with structures. *Comput. Geosci.* **231**, 5351-5373 (2015).
27. Meier, T., Rybacki, E., Reinicke, A., Dresen, G.: Influence of borehole diameter on the formation of borehole breakouts in black shale. *International Journal of Rock Mechanics and Mining Sciences.* **62**, 7485 (2013). <http://dx.doi.org/10.1016/j.ijrmm.2013.03.012>
28. Mori, T., Tanaka K.: Average stress in matrix and average elastic energy of materials with misfitting inclusions. *Acta Metallurgica*, **21** (1973).
29. Mortazavi, B., Baniassadi, M., Bardon, J., Ahzi, S.: Modeling of two-phase random composite materials by finite element, MoriTanaka and strong contrast methods. *Composites: Part B.* **45**, 1117-1125 (2013).
30. Moussaddy, H., Theriault, D., Lvesque, M.: A numerical approximation to the elastic properties of shpere reinforced composite. In: *The 19th International Conference on Composite Materials* (2013).
31. Naraghia, M.E., Javadpour, F.: A stochastic permeability model for the shale-gas systems. *International Journal of Coal Geology.* **140**, 111-124 (2015). <http://dx.doi.org/10.1016/j.coal.2015.02.004>

32. Onoda, G.Y., Liniger, E.G.: Random loose packings of uniform spheres and the dilatancy onset. *Physical Review Letters*. **64**(22), 2727-2730 (1990).
33. Ortega, J.A., Ulm, F.J., Abousleiman, Y.N.: The effect of the nanogranular nature of shale on their poroelastic behavior. *Acta Geotechnica*. **2**, 155182 (2007). DOI: 10.1007/s11440-007-0038-8
34. Sayers, C.M.: The elastic anisotropy of shale. *Journal of Geophysical Research*. **99**, B1, 767-774 (1994).
35. Segurado, J., Llorca, J.: A numerical approximation to the elastic properties of sphere reinforced composite. *Journal of the Mechanics and Physics of Solids*. **50**, 2107-2121 (2002).
36. Schmauder, S., Weber, U., Soppa, E.: Computational micromechanics of heterogeneous materials. *Key Engineering Materials*. **251-252**, 415-422 (2003).
37. Shen, W.Q., Shao, J.F., Kondo, D., Gatmiri, B.: A micromacro model for clayey rocks with a plastic compressible porous matrix. *International Journal of Plasticity*. **36**, 64-85 (2012). DOI: doi.org/10.1016/j.ijplas.2012.03.006
38. Shen, W.Q., Kondo, D., Dormieux, L., Shao, J.F.: A closed-form three scale model for ductile rocks with a plastically compressible porous matrix. *Mechanics of Materials*. **59**, 73-86 (2013).
39. Sierra, R., Tran M.H., Abousleiman, Y.N., Slatt R.M.: Woodford Shale Mechanical Properties and the Impacts of Lithofacies. In: the 44th US Rock Mechanics Symposium, ARMA 10-461 (2010).
40. Stransky, J., Vorel, J., Zeman, J., Sejnoha, M.: Mori-Tanaka based estimates of effective thermal conductivity of various engineering materials. *Micromachines*. **2**, 129-149 (2011). DOI:10.3390/mi2020129
41. Sulsky, D., Chen, Z., Schreyer, H.L.: A particle method for history-dependent materials. *Computer Methods in Applied Mechanics and Engineering*. 118(1-2), 179-196 (1994). DOI: 10.1016/0045-7825(94)90112-0
42. Sulsky, D., Schreyer, H.L.: Axisymmetric form of the material point method with applications to upsetting and Taylor impact problems. *Computer Methods in Applied Mechanics and Engineering*. **139**(1-4), 409-429 (1996). [http://dx.doi.org/10.1016/S0045-7825\(96\)01091-2](http://dx.doi.org/10.1016/S0045-7825(96)01091-2)
43. Ulm, F.J., Abousleiman, Y.: The nanogranular nature of shale. *Acta Geotechnica*. **1**, 77-88 (2006). DOI: 10.1007/s11440-006-0009-5
44. Vasin, R.N., Wenk, H.R., Kanitpanyacharoen, W., Matthies, S., Wirth, R.: Elastic anisotropy modeling of Kimmeridge shale. *Journal of Geophysical Research: Solid Earth*. **118**, 3931-3956 (2013). DOI:10.1002/jgrb.50259
45. Whitaker, M.L., Liu, W., Wang, L., Li, B.: Acoustic velocities and elastic properties of pyrite (FeS₂) to 9.6 GPa. *Journal of Earth Science*. **21**, 792-80 (2010). DOI: 10.1007/s12583-010-0115-z
46. Wiecekowsk, Z.: The material point method in large strain engineering problems. *Computer Methods in Applied Mechanics and Engineering*, 193:44174438 2004. DOI: 10.1016/j.cma.2004.01.035
47. Zaoui, A.: Continuum micromechanics: survey. *Journal of Engineering Mechanics*. **128**(8), 808-816 (2002). DOI: 10.1061/(ASCE)0733-9399(2002)128:8(808)
48. Zeszotarski, J.C., Chromik, R.R., Vinci, R.P., Messmer, M.C., Michels R., Larsen J.W.: Imaging and mechanical property measurements of kerogen via nanoindentation. *Geochimica et Cosmochimica Acta*. **68**, 4113-4119 (2004). DOI:10.1016/j.gca.2003.11.031
49. Zheng, Q.S., Du, D.X.: An explicit and universally applicable estimate for the effective properties of multiphase composites which accounts for inclusion distribution. *Journal of the Mechanics and Physics of Solids*. **49**, 2765-2788 (2001).
50. Zhu, Y., Xu, S., Payne, M., Martinez, A., Liu, E., Harris, C., Bandyopadhyay, K.: Improved rock-physics model for shale gas reservoirs. 82nd SEG Meeting Expanded Abstracts 0927 (2012).

A Appendix

A.1 Hill's tensor

For the case of local and global isotropic behaviour with spherical inclusions, the Hill's tensor is obtained as follows:

$$\mathbb{P}_{I_r}^0 = \frac{\beta_0}{2\mu_0} \mathbb{K} + \frac{\alpha_0}{3\kappa_0} \mathbb{J} \quad (30)$$

$$\alpha_0 = \frac{3\kappa_0}{3\kappa_0 + 4\mu_0} \quad (31)$$

$$\beta_0 = \frac{6(\kappa_0 + 2\mu_0)}{5(3\kappa_0 + 4\mu_0)} \quad (32)$$

where κ_0 and μ_0 are the clay matrix bulk and shear moduli, respectively. \mathbb{K} and \mathbb{J} denote the spherical and deviatoric isotropic operators which are defined as follows:

$$\mathbb{J} = \frac{1}{3} I \times I \quad (33)$$

$$\mathbb{K} = \mathbb{I} - \mathbb{J} \quad (34)$$

where I and \mathbb{I} are the second and forth order identity tensors, respectively.

A.2 GSCS' shear modulus

For a composite with isotropic matrix and spherical inclusions, the GSCS shear modulus can be expressed using the following three constants:

$$\begin{aligned}
 A = & 8\left(\frac{\mu_i}{\mu_0} - 1\right)(4 - 5v_0)\eta_1 f_i^{\frac{10}{3}} - 2\left(63\left(\frac{\mu_i}{\mu_0} - 1\right)\eta_2 + 2\eta_1\eta_3\right)f_i^{\frac{7}{3}} \\
 & + 252\left(\frac{\mu_i}{\mu_0} - 1\right)\eta_2\eta_3 f_i^{\frac{5}{3}} - 50\left(\frac{\mu_i}{\mu_0} - 1\right)(7 - 12v_0 + 8v_0^2)\eta_2 f_i \\
 & + 4(7 - 10v_0)\eta_2\eta_3
 \end{aligned} \tag{35}$$

$$\begin{aligned}
 B = & -4\left(\frac{\mu_i}{\mu_0} - 1\right)(1 - 5v_0)\eta_1 f_i^{\frac{10}{3}} + 4\left(63\left(\frac{\mu_i}{\mu_0} - 1\right)\eta_2 + 2\eta_1\eta_3\right)f_i^{\frac{7}{3}} \\
 & - 504\left(\frac{\mu_i}{\mu_0} - 1\right)\eta_2\eta_3 f_i^{\frac{5}{3}} + 150\left(\frac{\mu_i}{\mu_0} - 1\right)(3 - v_0)v_0\eta_2 f_i \\
 & + 3(15v_0 - 7)\eta_2\eta_3
 \end{aligned} \tag{36}$$

$$\begin{aligned}
 C = & 4\left(\frac{\mu_i}{\mu_0} - 1\right)(5v_0 - 7)\eta_1 f_i^{\frac{10}{3}} - 2\left(63\left(\frac{\mu_i}{\mu_0} - 1\right)\eta_2 + 2\eta_1\eta_3\right)f_i^{\frac{7}{3}} \\
 & + 252\left(\frac{\mu_i}{\mu_0} - 1\right)\eta_2\eta_3 f_i^{\frac{5}{3}} + 25\left(\frac{\mu_i}{\mu_0} - 1\right)(v_0^2 - 7)\eta_2 f_i \\
 & - (7 + 5v_0)\eta_2\eta_3
 \end{aligned} \tag{37}$$

with

$$\eta_1 = \left(\frac{\mu_i}{\mu_0} - 1\right)(49 - 50v_i v_0) + 35\left(\frac{\mu_i}{\mu_0}\right)(v_i - 2v_0) + 35(2v_i - v_0) \tag{38}$$

$$\eta_2 = 5v_i\left(\frac{\mu_i}{\mu_0} - 8\right) + 7(\mu_i + \mu_0 + 4) \tag{39}$$

$$\eta_3 = \left(\frac{\mu_i}{\mu_0}\right)(8 - 10v_0) + (7 - 5v_0) \tag{40}$$

where μ is the shear modulus, v is the Poisson's ratio, f is the volume fraction and the subscripts 0 and i refer to the matrix and inclusions, respectively.